

Communication

# Sensing Characteristics of SARS-CoV-2 Spike Protein Using Aptamer-Functionalized Si-Based Electrolyte-Gated Field-Effect Transistor (EGT)

Seonghwan Shin <sup>1</sup>, Sangwon Kim <sup>2</sup> , Wonyeong Choi <sup>1</sup> , Jeonghyeon Do <sup>1</sup> , Jongmin Son <sup>1</sup> , Kihyun Kim <sup>3</sup> , Sungkey Jang <sup>2</sup>  and Jeong-Soo Lee <sup>1,\*</sup> 

<sup>1</sup> Department of Electrical Engineering, Pohang University of Science and Technology (POSTECH), Pohang 37673, Republic of Korea; ssh3290a@postech.ac.kr (S.S.); pathfinder@postech.ac.kr (W.C.); toaru124@postech.ac.kr (J.D.); jmson@postech.ac.kr (J.S.)

<sup>2</sup> Department of Life Sciences, Pohang University of Science and Technology (POSTECH), Pohang 37673, Republic of Korea; ksw5758@postech.ac.kr (S.K.); sungkey@postech.ac.kr (S.J.)

<sup>3</sup> Division of Electronics Engineering, Jeonbuk National University, Jeonju 54896, Republic of Korea; kihyun.kim@jbnu.ac.kr

\* Correspondence: ljs6951@postech.ac.kr

**Abstract:** The sensing responses of SARS-CoV-2 spike protein using top-down-fabricated Si-based electrolyte-gated transistors (EGTs) have been investigated. An aptamer was employed as a receptor for the SARS-CoV-2 spike protein. The EGT demonstrated excellent intrinsic characteristics and higher sensitivity in the subthreshold regime compared to the linear regime. The limit of detection (LOD) was achieved as low as 0.94 pg/mL and 20 pg/mL for the current and voltage sensitivity, respectively. To analyze the sensing responses of EGT in detecting the aptamer-SARS-CoV-2 spike protein conjugate, a lumped-capacitive model with the presence of an effective dipole potential and an effective capacitance of the functionalized layer component was employed. The aptamer-functionalized EGT showed high sensitivity even in 10 mM phosphate-buffered saline (PBS) solution. These results suggest that Si-based EGTs are a highly promising method for detecting SARS-CoV-2 spike proteins.



**Citation:** Shin, S.; Kim, S.; Choi, W.; Do, J.; Son, J.; Kim, K.; Jang, S.; Lee, J.-S. Sensing Characteristics of SARS-CoV-2 Spike Protein Using Aptamer-Functionalized Si-Based Electrolyte-Gated Field-Effect Transistor (EGT). *Biosensors* **2024**, *14*, 124. <https://doi.org/10.3390/bios14030124>

Received: 26 December 2023

Revised: 17 February 2024

Accepted: 22 February 2024

Published: 26 February 2024



**Copyright:** © 2024 by the authors. Licensee MDPI, Basel, Switzerland. This article is an open access article distributed under the terms and conditions of the Creative Commons Attribution (CC BY) license (<https://creativecommons.org/licenses/by/4.0/>).

**Keywords:** EGT; aptamer; BioFET; SARS-CoV-2; COVID-19

## 1. Introduction

Severe Acute Respiratory Syndrome Coronavirus 2 (SARS-CoV-2) represents a virulent human infectious disease that can cause profound respiratory distress. The World Health Organization (WHO) declared the SARS-CoV-2 outbreak a pandemic and global health emergency on 11 March 2020 [1]. SARS-CoV-2 has a positive-stranded RNA genome that encodes four structural proteins: a spike surface glycoprotein (S), an envelope protein (E), a matrix protein (M), and a nucleocapsid protein (N) [2]. Among these structural proteins, the spike protein is the most reliable biomarker [3,4]. The spike protein is expressed as a trimer on the virus surface, consisting of two subunits, S1 and S2, and plays a crucial role in receptor recognition and cell membrane fusion [5]. The S1 subunit contains a receptor-binding domain (RBD) that recognizes and attaches to the Angiotensin-Converting Enzyme 2 (ACE2) receptor, while the S2 subunit mediates viral cell membrane fusion. The SARS-CoV-2 spike trimer (S1 + S2) protein offers an enhanced biological model compared to the monomeric spike RBD protein or the single S1 subunit.

Real-time polymerase chain reaction (RT-PCR) is recognized as a gold standard for diagnosing SARS-CoV-2 [6,7]. However, this approach is unsuitable for point-of-care testing because it requires specialized laboratories, sophisticated and expensive equipment, and trained personnel. Alternatively, several other methods, including electrochemical techniques [8,9], fluorescence [10,11], and impedance [12,13], have been demonstrated.

Among these, biosensor field-effect transistors (BioFETs) have emerged as a promising approach due to their low cost, ultra-sensitivity, and label-free detection [14–16]. In conventional BioFETs, the receptor is attached to the channel surface and combined with the target [17,18]. The output drain current of these BioFETs varies with the potential generated by the receptor–target conjugates.

Recently, electrolyte-gated transistors (EGTs) have been fabricated and analyzed using conducting polymer films as their channel materials to detect SARS-CoV-2 [19,20]. The utilization of a significant gate area as a functionalized surface increases the probability of binding events. However, for commercialization, organic EGTs should overcome some disadvantages compared to Si-based EGTs, such as environmental susceptibility, high-voltage operation, and difficulties integrating into existing Si-based devices in complex signal processing systems [21,22].

Aptamers, which are artificially produced single-stranded molecules of DNA or RNA, have high affinity and specificity for binding to target molecules such as proteins or small molecules [23,24]. Due to their smaller size, aptamers are less susceptible to interference from charged molecules in an electrolyte, resulting in a decreased Debye screening effect. It allows aptamers to maintain their binding affinity even in high salt concentrations or complex sample matrices, making them a promising tool for biosensing applications in real-world settings.

Here, we demonstrate the highly sensitive detection of SARS-CoV-2 spike protein (SC2) using aptamer-functionalized Si-EGT. The sensing behaviors under different operating regimes are investigated to achieve higher sensitivity. Furthermore, a lump-capacitive model is applied to analyze the characteristics of the aptamer–SC2 in EGT devices. The influence of buffer concentration and the non-specific binding test are also evaluated.

## 2. Materials and Methods

### 2.1. Fabrication of Si-Based EGT

Here, we demonstrate the ultrasensitive detection of SARS-CoV-2 spike protein (SC2) using aptamer-functionalized EGT. The sensing behaviors under different operating regimes are investigated to achieve higher sensitivity. Furthermore, a lump-capacitive model is applied to analyze the characteristics of the aptamer–SC2 in EGT sensors. The influence of buffer concentration and the non-specific binding test are also evaluated.

Figure 1a shows the fabrication flow of a Si-based EGT using a top-down process. An 8-inch silicon-on-insulator (SOI) wafer (p-type,  $10 \Omega\text{-cm}$ , (100)), (Soitec, Isere, France) with a 100 nm top-Si and 400 nm buried oxide (BOX) was used. The active region was formed using I-line stepper lithography and an inductively coupled plasma reactive ion etching (ICP-RIE) process (DMS, Taiwan). Then, the channel region was formed using electron beam lithography (E-beam lithography) (Elionix, Tokyo, Japan) and the ICP-RIE process. The ion implantation ( $\text{As}$ ,  $5 \times 10^{15} \text{ cm}^{-2}$ ) was conducted onto the substrate, followed by rapid thermal annealing (RTA) (Mattson, Fremont, CA, USA) at  $1000 \text{ }^\circ\text{C}$  for 20 s. Then, 5 nm  $\text{SiO}_2$ , a gate dielectric, was grown using a high-temperature pyro furnace (Centrotherm, Blaubeuren, Germany) at  $800 \text{ }^\circ\text{C}$  5 min. Next, the contact pads and transmission lines were formed by depositing Ag/Ti (500 nm/50 nm) using an electron beam evaporator (KVT, Seoul, Republic of Korea) and a conventional lift-off process. Finally, an SU-8 photoresist (Kayaku Advanced Materials Inc., Tokyo, Japan) was passivated on the device to prevent any leakage current flow, excluding the gate ( $1550 \mu\text{m} \times 300 \mu\text{m}$ ) and a channel region ( $10 \mu\text{m} \times 10 \mu\text{m}$ ). Figure 1b shows an optical image of the fabricated device.

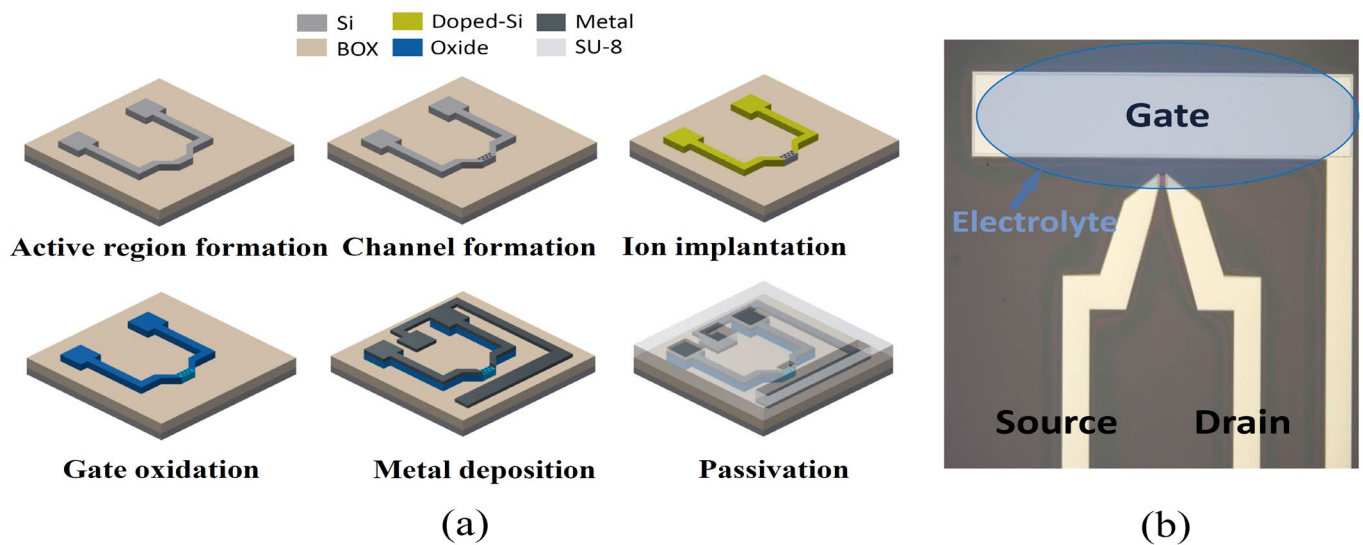


**Figure 1.** (a) Optical microscope image of fabricated Si-based EGT. Inset: SEM image of nanonet channel. (b) A schematic of fabrication flow.

### 2.2. Preparation of SARS-CoV-2 Spike Protein and Aptamer

The SARS-CoV-2 spike protein with S1 and S2 subunits was used, which is more similar to the real spike protein than using only the receptor-binding domain (RBD) or S1 subunit. Cells were cultured to produce protein, where Sf9 (*Spodoptera frugiperda*) cells were cultured in Sf 900 II SFM medium (Gibco, Waltham, MA, USA) with 0.1% penicillin/streptomycin mix and 0.2% amphotericin B (Sigma-Aldrich, St. Louis, MO, USA) in a shaking incubator at 27 °C. A baculovirus expression system was used to produce the spike protein. Baculovirus was generated by transfecting the recombinant baculovirus DNA into SF9 cells. Three days after infection, the medium was centrifuged at 6000 rpm and 10 min conditions to collect supernatant and purified by the Ni-affinity column purification method and size-exclusion chromatography. The aptamer was developed by VIRO-SELEX [25,26]. Several cycles of VIRO-SELEX were performed, and a pool of 11 cycles was chosen to analyze the sequence [27].

### 2.3. Immobilization of Aptamer on EGT

Firstly, devices were rinsed with ethanol and distilled water (DIW), followed by N<sub>2</sub> blowing. Then, to remove residual contaminants and increase the density of the hydroxyl group, UV/ozone treatment was conducted for 1.5 min. Next, the devices were exposed to 1% 3-aminopropyltriethoxysilane (APTES) (Sigma-Aldrich, St. Louis, MO, USA) vapors for 1 min at 50 °C to cover the surface with an amine group (-NH<sub>2</sub>). After removing the residual APTES by immediate dipping in anhydrous ethanol followed by N<sub>2</sub> blowing, the devices were immersed in 1 × PBS solution with 2.5% glutaraldehyde (GA) (Sigma-Aldrich, St. Louis, MO, USA) to form an aldehyde group on the surface [28–30]. Then, the devices were rinsed with 1 × PBS and DIW followed by N<sub>2</sub> blowing. Next, to immobilize the aptamer, the devices were exposed to 2.5 μL of 1 × PBS solution containing aptamers for 12 h at room temperature. Finally, the devices were exposed to 0.1% bovine serum albumin (BSA) (Sigma-Aldrich, St. Louis, MO, USA) in 1 × PBS for 90 min at room temperature to block the unreacted active sites to prevent non-specific binding.

### 2.4. Electrical Measurement Set-Up

A semiconductor analyzer (Keithley 4200-SCS, Tektronics, Beaverton, OR, USA) was utilized to characterize the drain current ( $I_D$ ) and gate voltage ( $V_G$ ) modulation generated by SARS-CoV-2 responses. All measurements were conducted with a source voltage ( $V_S$ ) of 0 V, drain voltage ( $V_D$ ) of 0.1 V, and  $V_G$  ranging from 0 V to 1 V with a 0.05 V step. A wide

concentration range of SARS-CoV-2 (SC2) from 33 pg/mL to 3.3 µg/mL was prepared in  $1 \times$  PBS solution. The measurement sequence was as follows: Initially, the  $I_D$ - $V_G$  curve of the aptamer-functionalized devices was characterized in a  $0.01 \times$  PBS solution. Next, the device was exposed to an SC2 spike protein solution ( $1 \times$  PBS, 2.5 µL) for 90 min at room temperature, followed by a rinse. Finally, the  $I_D$ - $V_G$  characterization was performed again in  $0.01 \times$  PBS solution.

### 3. Results

#### 3.1. Electrical Characteristics of Fabricated Si-Based EGT

Figure 2a shows a transfer curve (log-scale  $I_D$ - $V_G$ ) and output curve ( $I_D$ - $V_D$ , inset) of the fabricated Si-EGT, demonstrating excellent intrinsic characteristics, including a subthreshold swing ( $SS \equiv dV_G/d\log(I_D)$ ) of  $\sim 80$  mV/dec, threshold voltage ( $V_{TH}$ ) of 0.65 V, an on-off current ratio of  $\sim 10^7$ , and a gate leakage current ( $I_G$ ) of  $\sim 10^{-12}$  A. Figure 2b shows a representative transfer curve of the EGT with various concentrations of [SC2], ranging from the initial amount (no [SC2]) up to 3.3 µg/mL. The increase in [SC2] causes a negative shift in the transfer curves.

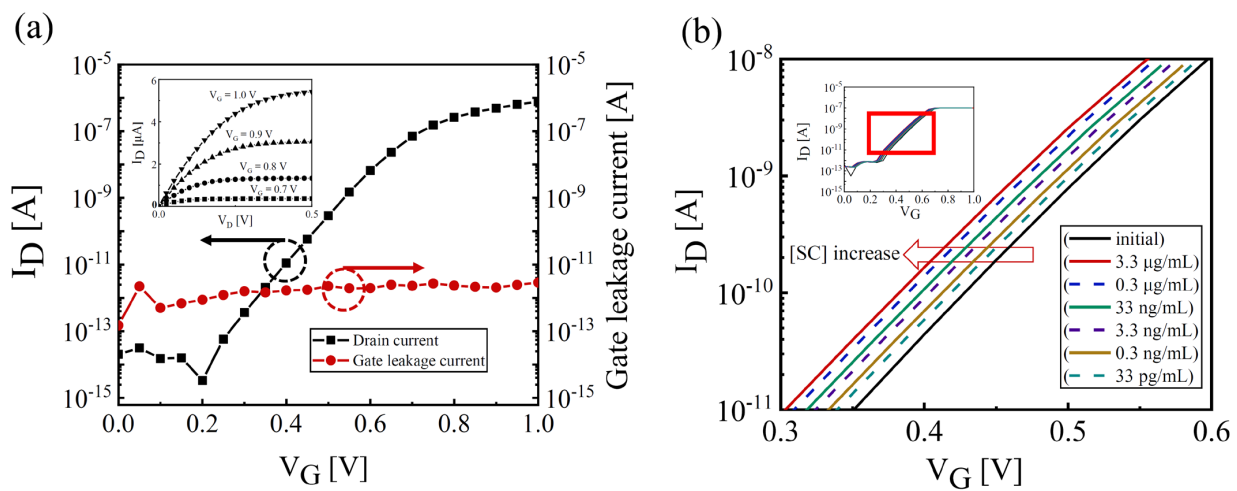


**Figure 2.** (a) A representative intrinsic transfer characteristics (Log ( $I_D$ ) vs.  $V_G$ ) and gate leakage characteristic of the fabricated EGT at  $V_D = 0.1$  V. The device was characterized in  $0.01 \times$  PBS solution. Inset: an output characteristic ( $I_D$  vs.  $V_D$ ) at fixed  $V_G$  ranging from 0.7 V~1.0 V. (b) A shift in the transfer curve with various [SC2] values. The inset shows the overall transfer curve. A compliance  $I_D$  of 100 nA was applied to ensure reproducibility and avoid degradation.

#### 3.2. Sensing Responses of the EGTs for the SC2 Detection

The current sensitivity ( $S_I$ ) and voltage sensitivity ( $S_V$ ) are typically defined as follows [31,32]:

$$S_I = \frac{I_{D\_SC2} - I_{D\_AP}}{I_{D\_AP}} \quad (1)$$

$$S_V = V_{G\_AP} - V_{G\_SC2} \quad (2)$$

where  $I_{D\_AP}$  and  $I_{D\_SC2}$  are the drain currents at a fixed  $V_{G\_AP}$  after aptamer immobilization and after SC2 exposure, respectively, and  $V_{G\_AP}$  and  $V_{G\_SC2}$  are the gate voltages at a fixed  $I_{D\_AP}$  after aptamer immobilization and after SC2 exposure, respectively.

Figure 3 shows the dependence of  $S_I$  and  $S_V$  on  $I_{D\_AP}$ . Both  $S_I$  and  $S_V$  show different behaviors as the operation shifts from the subthreshold regime ( $I_D < 10$  nA) to the linear regime ( $I_D > 10$  nA) through an increase in  $V_G$ . At a given SC2 exposure,  $S_I$  shows a constant behavior as  $I_{D\_AP}$  decreases in the subthreshold regime, while it radically reduces in the linear regime, as shown in Figure 3a. In contrast, the  $S_V$  has a constant behavior independent of  $I_{D\_AP}$  values. It suggests that the exposure to SC2 causes little degradation

to the devices with a lateral shift in the transfer curve from subthreshold to linear regimes. Thus, the Si-based EGTs should be operated in the subthreshold regime to achieve high sensitivity and low power consumption.

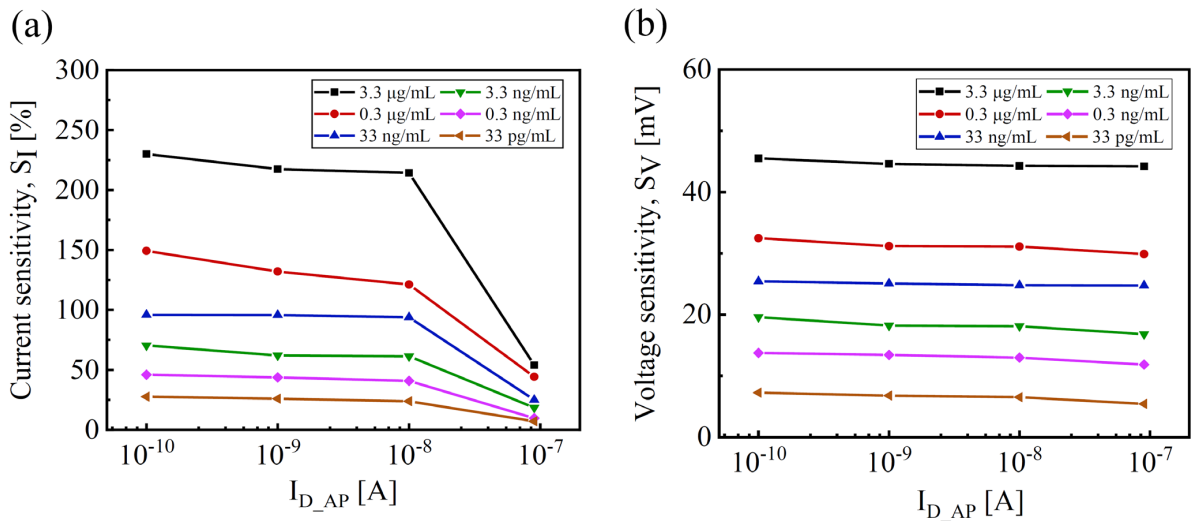


**Figure 3.** Dependence of sensitivities on the operation regimes: (a) average  $S_I$  vs.  $I_{D,AP}$  and (b) average  $S_V$  vs.  $I_{D,AP}$ .

Figure 4 shows  $S_I$  and  $S_V$  as a function of [SC2]. The logistic calibration curves were  $S_I = 376.2 \times [\text{SC2}]^{0.26} / (0.03 + [\text{SC2}]^{0.26})$  and  $S_V = 72.1 \times [\text{SC2}]^{0.2} / (0.06 + [\text{SC2}]^{0.2})$  [33,34]. The dynamic range was about four orders of magnitude from 33 pg/mL to 3.3 μg/mL of [SC2]. The LOD was determined using the three-sigma method with the fitting sensitivity equation and blank replicate data ( $1 \times \text{PBS}$  without [SC2]) [31,35]. The average of the blank replicate was as low as  $-9.3\%$  for  $S_I$  and  $-1.84 \text{ mV}$  for  $S_V$ , respectively, while the standard deviation of the blank replicate was as low as  $10.4\%$  for  $S_I$  and  $3.47 \text{ mV}$  for  $S_V$ , respectively. The extracted LOD was achieved as low as  $945 \text{ fg/mL}$  and  $20 \text{ pg/mL}$  for  $S_I$  and  $S_V$ , respectively. From the slope of the logistic fitted line in Figure 4, the SC2 sensitivities of  $50.8\%/\log [\text{SC2}]$  for  $S_I$  and  $7.9 \text{ mV}/\log [\text{SC2}]$  for  $S_V$  are extracted, respectively. These values are more than two times higher than the previous results (Table 1).

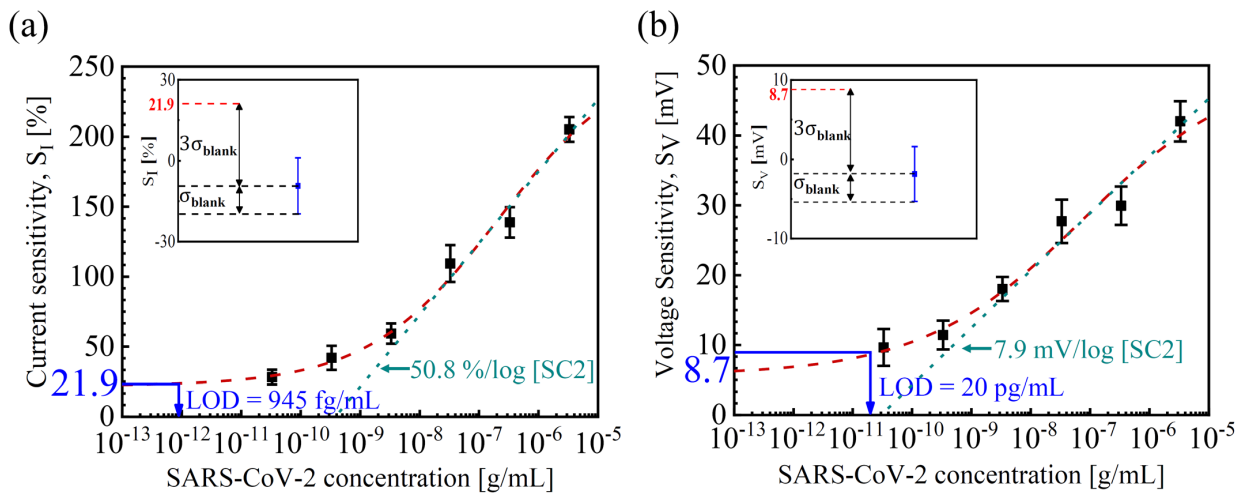


**Figure 4.** (a)  $S_I$  and (b)  $S_V$  vs. [SC2] at  $I_{D,AP} = 1 \text{ nA}$ . The red dashed lines represent the logistic fitted curves. The inset shows the  $S_I$  and  $S_V$  values obtained from blank samples without SC2 to calculate the LOD using the three-sigma method.

To further understand the sensing responses of EGT in detecting the aptamer–SC2 conjugate, a lumped-capacitive model with the presence of a dipole layer and a capacitive component was employed [19,36,37]. The binding factor  $\alpha$ , defined as the ratio of the aptamer sites bound with the SC2 molecules to the total aptamer sites, can be expressed as [33,36,38]

$$\alpha = \frac{N_{AP\_SC2}}{N_{AP}} = \frac{[SC2]^n}{(K + [SC2]^n)} \quad (3)$$

where  $N_{AP\_SC2}$  is the density of the aptamer–SC2 conjugates,  $N_{AP}$  is the density of total immobilized aptamers,  $K$  is related to the dissociation constant of the aptamer–SC2 binding, and  $n$  is a slope factor that indicates the cooperativity of SC2 binding.

After introducing SC2 to the aptamer-functionalized surface, it generates an effective dipole moment ( $V_{DP\_EFF}$ ) and an effective capacitance ( $C_{FN\_EFF}$ ).  $V_{DP\_EFF}$  can be expressed as follows [20,36,37]:

$$V_{DP\_EFF} = \frac{\alpha \cdot N_{AP} \cdot P_{DP}}{\epsilon_{DP}} \cong V_{DP\_GT} \quad (4)$$

where  $P_{DP}$  is the perpendicular component of the dipole moment,  $\epsilon_{DP}$  is the permittivity of the dipole layer, and  $V_{DP\_GT}$  is the dipole potentials at the gate electrode.  $V_{DP\_EFF}$  is mainly determined from the gate electrode since the gate area is ~5000 times larger than the channel area in the fabricated EGT device. The established  $V_{DP\_EFF}$  changes the flatband voltage, causing a shift in the  $I_D$  vs.  $V_G$  curve. The positive  $V_{DP\_EFF}$  reduces  $V_{TH}$  and shifts the transfer curve toward the negative  $V_G$  direction.

$C_{FN\_EFF}$  is related to the biomaterials on the channel and can be expressed as follows [36]:

$$C_{FN\_EFF} = C_{SC2\_CH} + (C_{SC2\_CH} + C_{AP\_CH}) \frac{K}{[SC2]^n} \quad (5)$$

where  $C_{SC2\_CH}$  and  $C_{AP\_CH}$  are the SC2 and aptamer capacitances per unit area at the channel.

Then,  $S_V$  is calculated using  $V_{DP\_EFF}$  and  $C_{FN\_EFF}$  as follows:

$$S_V = V_{DP\_EFF} + \frac{Q_S}{C_{FN\_EFF}} \quad (6)$$

where  $Q_S$  is the total charge density in the channel.

Figure 5 shows the  $|Q_S|$  versus  $S_V$  characteristics for different [SC2] values. For an n-type channel, the negative  $Q_S$  can be determined by summing the depletion charge, inversion charge, and interface trap charge in the channel [39,40].  $V_{DP\_EFF}$  and  $C_{FN\_EFF}$  are obtained from the y-intercept and reciprocal slope of the curves, respectively.

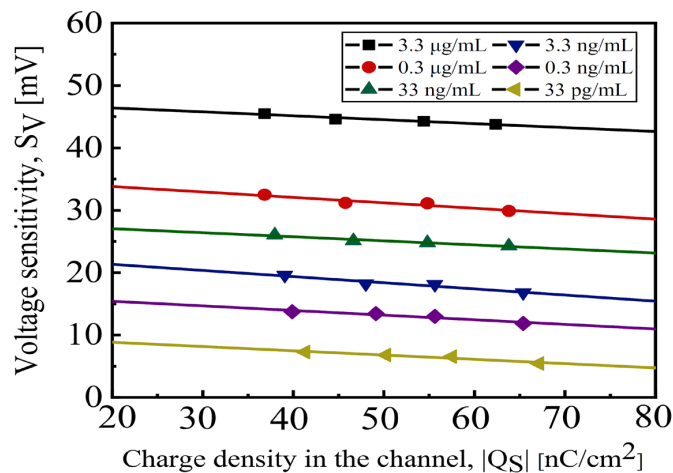
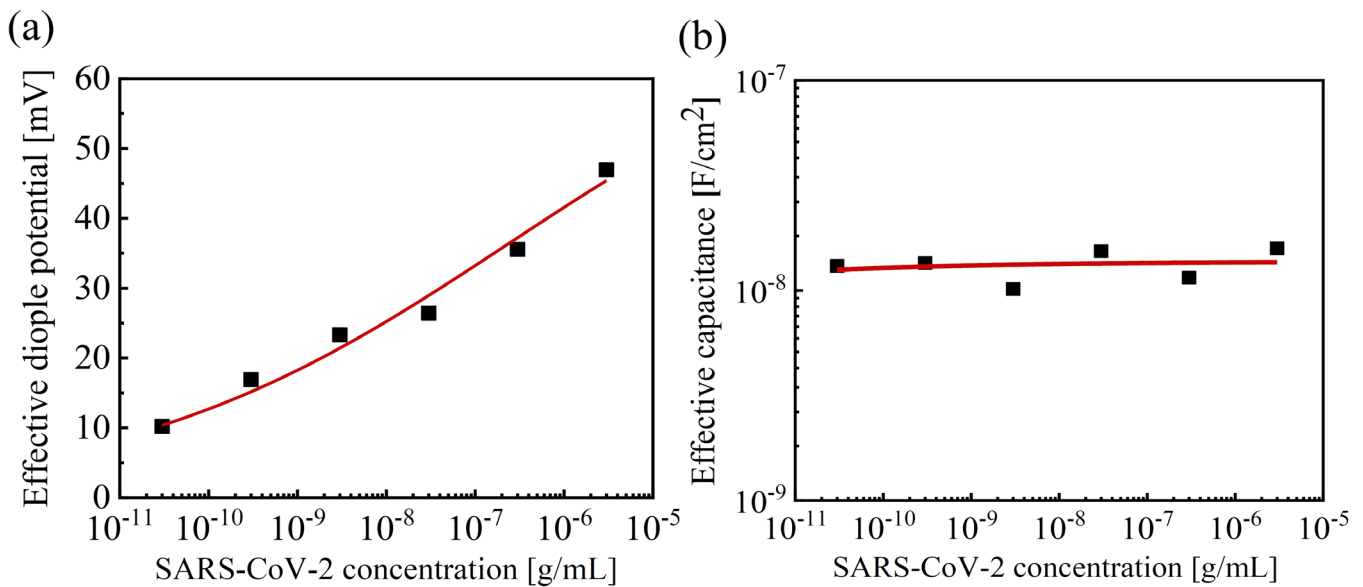


Figure 5.  $|Q_S|$  vs.  $S_V$  with various values of [SC2].

Figure 6a shows the relationship between  $V_{DP\_EFF}$  and [SC2]. The positive  $V_{DP\_EFF}$  is clearly proportional to [SC2], and the logistics calibration curve of  $V_{DP\_EFF}$  is obtained as  $V_{DP\_EFF} = 72.7 \times [SC2]^{0.2} / (0.047 + [SC2]^{0.2})$ . By utilizing equations (3), the binding factor  $\alpha$  can be calculated as  $\alpha = [SC2]^{0.2} / (4.7 \times 10^{-2} + [SC2]^{0.2})$  with  $K = 4.7 \times 10^{-2}$  and  $n = 0.2$ . A lower  $K$  value of the aptamer reaction, compared to the previous protein detection ( $K = 1.84 \times 10^{-3}$ ), indicates that the aptamer conjugate is more prone to dissociation than the peanut protein conjugates [36]. In Figure 6b, the extracted  $C_{FN\_EFF}$  is fitted as  $C_{FN\_EFF} = 1.37 \times 10^{-8} - 9.4 \times 10^{-12} \times [SC2]^{-0.2} \approx 1.37 \times 10^{-8}$  using the extracted  $K$  and  $n$  values. The [SC2] capacitance generates a constant  $C_{FN\_EFF}$  for various [SC2]. Thus, compared to previous protein detection [36], the binding characteristics in the channel are negligibly involved in the overall aptamer detection.



**Figure 6.** (a) The extracted effective dipole potential  $V_{DP\_EFF}$  and (b) effective capacitance  $C_{FN\_EFF}$  with various [SC2].

Debye screening is another crucial factor that can affect the sensing performance of BioFETs. It refers to the phenomenon in which charged ions in an electrolyte shield the electric charge of the conjugates [41–43]. The Debye length is the characteristic length scale over which the electrical potential of a charged molecule decays exponentially due to the surrounding ions in an electrolyte. When the Debye length is comparable to the distance between the channel surface and the conjugates, the electrostatic interaction is significantly weakened due to the shielding effect of the charged ions in the solution [44].

To assess the impact of Debye screening on the responses to SC2, three different PBS solutions ( $0.01 \times$ ,  $0.1 \times$ , and  $1 \times$  PBS) were prepared by diluting  $1 \times$  PBS with DI water. Figure 7 shows the measured  $S_I$  and  $S_V$  at different PBS concentrations using an exposure of 33 ng/mL SC2. Both sensitivities increased as the PBS concentration decreased. The  $S_I$  and  $S_V$  values were approximately 80% higher in  $0.01 \times$  PBS buffer than in  $1 \times$  PBS solution. Interestingly, our devices were capable of detecting [SC2] even in  $1 \times$  PBS solution, despite the larger [SC2] used compared to other SARS-CoV-2 spike proteins that typically consist of only a smaller S1 subunit and RBD [14,45].

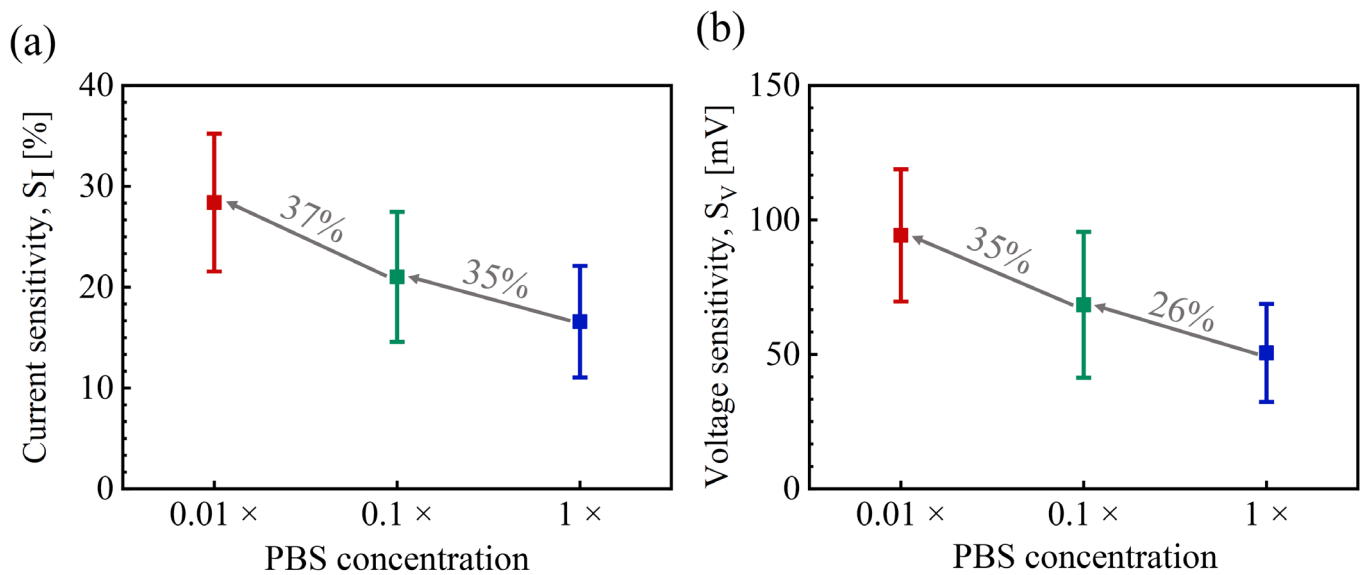


**Figure 7.** Dependence of (a)  $S_I$  and (b)  $S_V$  on the PBS concentrations.  $S_I$  was extracted at  $I_{D\_AP} = 1$  nA and  $[SC2] = 33$  ng/mL.

Figure 8 presents non-specific control experiments to confirm the selectivity to SC2. Various test samples, such as influenza B virus HA (hemagglutinin) protein and human coronavirus (HCoV-HKU1) spike protein, were exposed to high enough concentrations to confirm the specificity of the SARS-CoV-2 spike protein. The  $S_I$  and  $S_V$  values obtained from these biomolecules were sufficiently low and below 33 pg/mL of SC2, indicating that the sensitivity is specific to SC2 binding. In addition, when exposed to 3.3  $\mu$ g/mL of SC2, the unmodified EGT exhibited negligible  $S_I$  and  $S_V$ , indicating that the SC2 aptamers were successfully immobilized and could be used to evaluate the surface functionalization process.

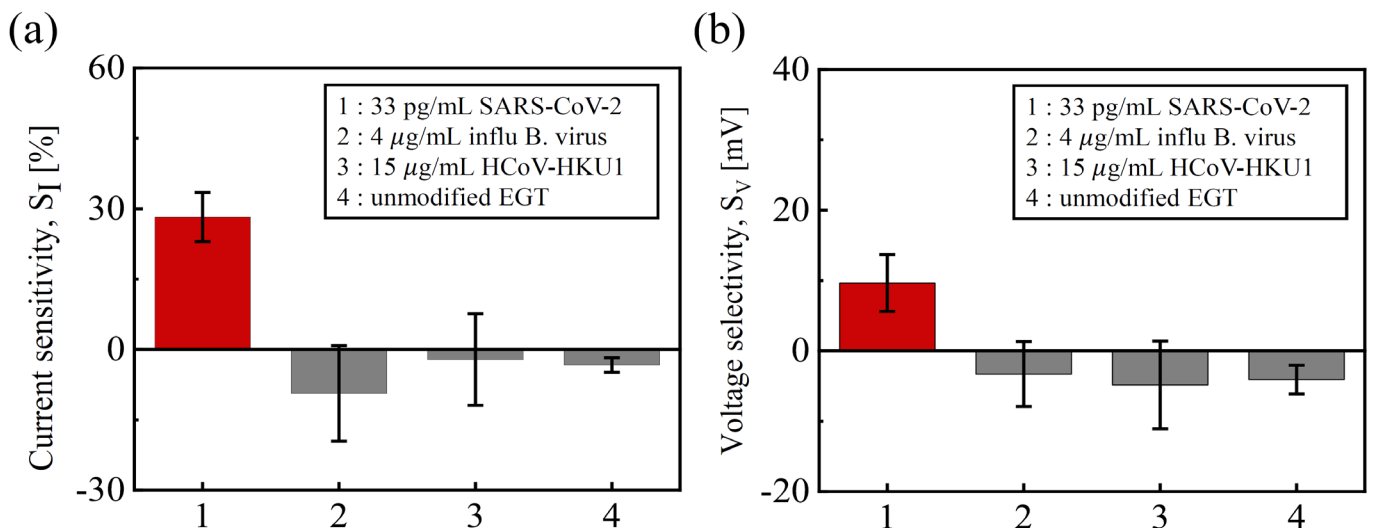


**Figure 8.** Selectivity tests of (a)  $S_I$  and (b)  $S_V$  with 4  $\mu$ g/mL influenza B virus, 15  $\mu$ g/mL HCoV-HKU1, and unmodified EGTs.

Table 1 compares the sensing performance of the EGT with previously reported sensors for detecting SC2. The Si-based EGT shows a significant improvement in both dynamic range and sensitivity.

**Table 1.** Comparison between various SC2 sensors.

Sensor Type	Biomarker	Dynamic Range	Sensitivity from $S_I$ (%/log [SC2])	Limit of Detection	Ref.
Paper-based electrochemical sensor	RBD	$10^3$ (1 ng/mL to 1 $\mu$ g/mL)	10.7	1 ng/mL	[46]
CNT-FET sensor	S1	$5 \times 10^4$ (0.1 fg/m to 5 pg/mL)	3.8	4.12 fg/mL	[47]
Graphene-FET sensor	S1	$10^4$ (1 fg/mL to 10 pg/mL)	16	1 fg/mL	[14]
Electrical-double-layer (EDL)-gated FET sensor	N protein	$10^3$ (0.4 ng/mL to 400 ng/mL)	4.6	0.34 ng/mL	[48]
Organic electrochemical transistor immuno-sensor	RBD	$10^6$ (1.4 pg/mL to 1.4 $\mu$ g/mL)	1.6	1.4 pg/mL	[49]
Si-based EGT	S1 + S2	$10^5$ (33 pg/mL to 3.3 $\mu$ g/mL)	50.8	945 fg/mL	This work

#### 4. Conclusions

We have successfully demonstrated the highly sensitive detection of SARS-CoV-2 spike protein using aptamer-functionalized Si-based EGTs. A lumped-capacitive model was utilized to analyze the aptamer–SC2 conjugates on the sensing performances in terms of dipole moments and capacitive components. The fabricated EGT showed higher sensitivities in the subthreshold regime, achieving LODs of 0.94 pg/mL and 20 pg/mL for current and voltage sensitivity, respectively. In addition, the EGT showed high sensitivity even in  $1 \times$  PBS solution. These results suggest that the Si-based EGTs using advanced microfabrication technology are promising in detecting SARS-CoV-2 spike proteins.

**Author Contributions:** Conceptualization, S.S.; methodology, S.S., S.K. and S.J.; validation, S.S. and J.-S.L.; investigation, S.S., W.C. and S.J.; data curation, J.D. and J.S.; writing—original draft preparation, S.S., K.K., J.S. and J.-S.L.; writing—review and editing, S.S. and J.-S.L.; supervision, J.-S.L.. All authors have read and agreed to the published version of the manuscript.

**Funding:** This research was supported by National R&D Program through the National Research Foundation of Korea (NRF) funded by the Ministry of Science and ICT (2020M3H2A107804514).

**Institutional Review Board Statement:** Not applicable.

**Informed Consent Statement:** Not applicable.

**Data Availability Statement:** Data are contained within the article.

**Conflicts of Interest:** The authors declare no conflicts of interest.

#### References

- WHO. *Novel Coronavirus (2019-nCoV) Situation Report*; WHO: Geneva, Switzerland, 2020.
- Wang, H.; Li, X.; Li, T.; Zhang, S.; Wang, L.; Wu, X.; Liu, J. The genetic sequence, origin, and diagnosis of SARS-CoV-2. *Eur. J. Clin. Microbiol. Infect. Dis.* **2020**, *39*, 1629–1635. [[CrossRef](#)] [[PubMed](#)]
- Yao, H.; Song, Y.; Chen, Y.; Wu, N.; Xu, J.; Sun, C.; Zhang, J.; Weng, T.; Zhang, Z.; Wu, Z.; et al. Molecular Architecture of the SARS-CoV-2 Virus. *Cell* **2020**, *183*, 730–738.e713. [[CrossRef](#)] [[PubMed](#)]
- Zhao, P.; Praissman, J.L.; Grant, O.C.; Cai, Y.; Xiao, T.; Rosenbalm, K.E.; Aoki, K.; Kellman, B.P.; Bridger, R.; Barouch, D.H.; et al. Virus-Receptor Interactions of Glycosylated SARS-CoV-2 Spike and Human ACE2 Receptor. *Cell Host Microbe* **2020**, *28*, 586–601.e6. [[CrossRef](#)] [[PubMed](#)]
- Xiaojie, S.; Yu, L.; Lei, Y.; Guang, Y.; Min, Q. Neutralizing antibodies targeting SARS-CoV-2 spike protein. *Stem Cell Res.* **2020**, *50*, 102125. [[CrossRef](#)] [[PubMed](#)]
- Vasudevan, H.N.; Xu, P.; Servellita, V.; Miller, S.; Liu, L.; Gopez, A.; Chiu, C.Y.; Abate, A.R. Digital droplet PCR accurately quantifies SARS-CoV-2 viral load from crude lysate without nucleic acid purification. *Sci. Rep.* **2021**, *11*, 780. [[CrossRef](#)] [[PubMed](#)]
- Carter, L.J.; Garner, L.V.; Smoot, J.W.; Li, Y.; Zhou, Q.; Saveson, C.J.; Sasso, J.M.; Gregg, A.C.; Soares, D.J.; Beskid, T.R.; et al. Assay Techniques and Test Development for COVID-19 Diagnosis. *ACS Cent. Sci.* **2020**, *6*, 591–605. [[CrossRef](#)]

8. Kaushik, A.K.; Dhau, J.S.; Gohel, H.; Mishra, Y.K.; Kateb, B.; Kim, N.Y.; Goswami, D.Y. Electrochemical SARS-CoV-2 Sensing at Point-of-Care and Artificial Intelligence for Intelligent COVID-19 Management. *ACS Appl. Bio Mater.* **2020**, *3*, 7306–7325. [[CrossRef](#)] [[PubMed](#)]
9. Idili, A.; Parolo, C.; Alvarez-Diduk, R.; Merkoci, A. Rapid and Efficient Detection of the SARS-CoV-2 Spike Protein Using an Electrochemical Aptamer-Based Sensor. *ACS Sens.* **2021**, *6*, 3093–3101. [[CrossRef](#)]
10. Zhou, C.; Lin, C.; Hu, Y.; Zan, H.; Xu, X.; Sun, C.; Zou, H.; Li, Y. Sensitive fluorescence biosensor for SARS-CoV-2 nucleocapsid protein detection in cold-chain food products based on DNA circuit and g-CNQDs@Zn-MOF. *Lebensm. Wiss. Technol.* **2022**, *169*, 114032. [[CrossRef](#)]
11. Li, D.; Zhou, Z.; Sun, J.; Mei, X. Prospects of NIR fluorescent nanosensors for green detection of SARS-CoV-2. *Sens. Actuators B Chem.* **2022**, *362*, 131764. [[CrossRef](#)]
12. Amouzadeh Tabrizi, M.; Acedo, P. An Electrochemical Impedance Spectroscopy-Based Aptasensor for the Determination of SARS-CoV-2-RBD Using a Carbon Nanofiber-Gold Nanocomposite Modified Screen-Printed Electrode. *Biosensors* **2022**, *12*, 142. [[CrossRef](#)]
13. Cho, H.; Shim, S.; Cho, W.W.; Cho, S.; Baek, H.; Lee, S.M.; Shin, D.S. Electrochemical Impedance-Based Biosensors for the Label-Free Detection of the Nucleocapsid Protein from SARS-CoV-2. *ACS Sens.* **2022**, *7*, 1676–1684. [[CrossRef](#)] [[PubMed](#)]
14. Seo, G.; Lee, G.; Kim, M.J.; Baek, S.H.; Choi, M.; Ku, K.B.; Lee, C.S.; Jun, S.; Park, D.; Kim, H.G.; et al. Rapid Detection of COVID-19 Causative Virus (SARS-CoV-2) in Human Nasopharyngeal Swab Specimens Using Field-Effect Transistor-Based Biosensor. *ACS Nano* **2020**, *14*, 5135–5142. [[CrossRef](#)] [[PubMed](#)]
15. Shahdeo, D.; Chauhan, N.; Majumdar, A.; Ghosh, A.; Gandhi, S. Graphene-Based Field-Effect Transistor for Ultrasensitive Immunosenesing of SARS-CoV-2 Spike S1 Antigen. *ACS Appl. Bio Mater.* **2022**, *5*, 3563–3572. [[CrossRef](#)] [[PubMed](#)]
16. Chen, M.; Cui, D.; Zhao, Z.; Kang, D.; Li, Z.; Albawardi, S.; Alsageer, S.; Alamri, F.; Alhazmi, A.; Amer, M.R.; et al. Highly sensitive, scalable, and rapid SARS-CoV-2 biosensor based on In(2)O(3) nanoribbon transistors and phosphatase. *Nano Res.* **2022**, *15*, 5510–5516. [[CrossRef](#)] [[PubMed](#)]
17. Kim, K.; Park, C.; Kwon, D.; Kim, D.; Meyyappan, M.; Jeon, S.; Lee, J.S. Silicon nanowire biosensors for detection of cardiac troponin I (cTnI) with high sensitivity. *Biosens. Bioelectron.* **2016**, *77*, 695–701. [[CrossRef](#)] [[PubMed](#)]
18. Hideshima, S.; Sato, R.; Inoue, S.; Kuroiwa, S.; Osaka, T. Detection of tumor marker in blood serum using antibody-modified field effect transistor with optimized BSA blocking. *Sens. Actuators B Chem.* **2012**, *161*, 146–150. [[CrossRef](#)]
19. Nguyen, T.T.K.; Nguyen, T.N.; Anquetin, G.; Reisberg, S.; Noel, V.; Mattana, G.; Touzeau, J.; Barbault, F.; Pham, M.C.; Piro, B. Triggering the Electrolyte-Gated Organic Field-Effect Transistor output characteristics through gate functionalization using diazonium chemistry: Application to biodetection of 2,4-dichlorophenoxyacetic acid. *Biosens. Bioelectron.* **2018**, *113*, 32–38. [[CrossRef](#)] [[PubMed](#)]
20. Lin, P.; Luo, X.; Hsing, I.M.; Yan, F. Organic electrochemical transistors integrated in flexible microfluidic systems and used for label-free DNA sensing. *Adv. Mater.* **2011**, *23*, 4035–4040. [[CrossRef](#)]
21. Bobbert, P.A.; Sharma, A.; Mathijssen, S.G.; Kemerink, M.; de Leeuw, D.M. Operational stability of organic field-effect transistors. *Adv. Mater.* **2012**, *24*, 1146–1158. [[CrossRef](#)]
22. Sirringhaus, H. Reliability of Organic Field-Effect Transistors. *Adv. Mater.* **2009**, *21*, 3859–3873. [[CrossRef](#)]
23. Shukoor, M.I.; Altman, M.O.; Han, D.; Bayrac, A.T.; Ocoy, I.; Zhu, Z.; Tan, W. Aptamer-nanoparticle assembly for logic-based detection. *ACS Appl. Mater. Interfaces* **2012**, *4*, 3007–3011. [[CrossRef](#)] [[PubMed](#)]
24. Hong, K.L.; Sooter, L.J. Single-Stranded DNA Aptamers against Pathogens and Toxins: Identification and Biosensing Applications. *Biomed. Res. Int.* **2015**, *2015*, 419318. [[CrossRef](#)] [[PubMed](#)]
25. Kwon, J.; Narayan, C.; Kim, C.; Han, M.J.; Kim, M.; Jang, S.K. Development of a Subtype-Specific Diagnostic System for Influenza Virus H3N2 Using a Novel Virus-Based Systematic Evolution of Ligands by Exponential Enrichment (Viro-SELEX). *J. Biomed. Nanotechnol.* **2019**, *15*, 1609–1621. [[CrossRef](#)] [[PubMed](#)]
26. Narayan, C.; Kwon, J.; Kim, C.; Kim, S.J.; Jang, S.K. Virus-based SELEX (viro-SELEX) allows development of aptamers targeting knotty proteins. *Analyst* **2020**, *145*, 1473–1482. [[CrossRef](#)] [[PubMed](#)]
27. Rahman, M.S.; Han, M.J.; Kim, S.W.; Kang, S.M.; Kim, B.R.; Kim, H.; Lee, J.O.; et al. Structure-Guided Development of Bivalent Aptamers Blocking SARS-CoV-2 Infection. *Molecules* **2023**, *28*, 4645. [[CrossRef](#)] [[PubMed](#)]
28. Farrow, T.; Laumier, S.; Sandall, I.; van Zalinge, H. An Aptamer-Functionalised Schottky-Field Effect Transistor for the Detection of Proteins. *Biosensors* **2022**, *12*, 137. [[CrossRef](#)]
29. Gunda, N.S.K.; Singh, M.; Norman, L.; Kaur, K.; Mitra, S.K. Optimization and characterization of biomolecule immobilization on silicon substrates using (3-aminopropyl)triethoxysilane (APTES) and glutaraldehyde linker. *Appl. Surf. Sci.* **2014**, *305*, 522–530. [[CrossRef](#)]
30. Honnali, S.K.; Srinivasa Raghavan, V.; Ashwath, R.; Saravanavel, G.; Gunasekhar, K.R.; Sambandan, S.; Gorthi, S.S.; O'Driscoll, B.; Jenkins, D. Aptamer Functionalized ZnO Thin-Film Transistor Based Multiplexed Detection of Pb and E. coli in Water. *IEEE Sens. J.* **2022**, *22*, 21209–21217. [[CrossRef](#)]
31. Gao, A.; Lu, N.; Wang, Y.; Li, T. Robust ultrasensitive tunneling-FET biosensor for point-of-care diagnostics. *Sci. Rep.* **2016**, *6*, 22554. [[CrossRef](#)]
32. Shoorideh, K.; Chui, C.O. Optimization of the Sensitivity of FET-Based Biosensors via Biasing and Surface Charge Engineering. *IEEE Trans. Electron. Devices* **2012**, *59*, 3104–3110. [[CrossRef](#)]

33. Tajima, N.; Takai, M.; Ishihara, K. Significance of antibody orientation unraveled: Well-oriented antibodies recorded high binding affinity. *Anal. Chem.* **2011**, *83*, 1969–1976. [[CrossRef](#)] [[PubMed](#)]
34. Tschmelak, J.; Kumpf, M.; Kappel, N.; Proll, G.; Gauglitz, G. Total internal reflectance fluorescence (TIRF) biosensor for environmental monitoring of testosterone with commercially available immunochemistry: Antibody characterization, assay development and real sample measurements. *Talanta* **2006**, *69*, 343–350. [[CrossRef](#)] [[PubMed](#)]
35. Armbruster, D.; Pry, T. Limit of blank, limit of detection and limit of quantitation. *Clin. BioChem.* **2008**, *29*, S49–S52.
36. Kim, D.; Choi, W.; Shin, S.; Park, J.; Kim, K.; Jin, B.; Lee, J.-S. Lumped-Capacitive Modeling and Sensing Characteristics of an Electrolyte-Gated FET Biosensor for the Detection of the Peanut Allergen. *IEEE Access* **2021**, *9*, 168922–168929. [[CrossRef](#)]
37. Macchia, E.; Manoli, K.; Holzer, B.; Di Franco, C.; Ghittorelli, M.; Torricelli, F.; Alberga, D.; Mangiatordi, G.F.; Palazzo, G.; Scamarcio, G.; et al. Single-molecule detection with a millimetre-sized transistor. *Nat. Commun.* **2018**, *9*, 3223. [[CrossRef](#)] [[PubMed](#)]
38. Kurganov, B.I.; Lobanov, A.V.; Borisov, I.A.; Reshetilov, A.N. Criterion for Hill equation validity for description of biosensor calibration curves. *Anal. Chem. Acta* **2001**, *19*, 11–19. [[CrossRef](#)]
39. He, J.; Liu, F.; Bian, W.; Feng, J.; Zhang, J.; Zhang, X. An approximate carrier-based compact model for fully depleted surrounding-gate MOSFETs with a finite doping body. *Semicond. Sci. Technol.* **2007**, *22*, 671–677. [[CrossRef](#)]
40. Lee, S. Bias-dependent subthreshold characteristics and interface states in disordered semiconductor thin-film transistors. *Semicond. Sci. Technol.* **2019**, *34*, 11LT01. [[CrossRef](#)]
41. Gao, A.; Lu, N.; Wang, Y.; Dai, P.; Li, T.; Gao, X.; Wang, Y.; Fan, C. Enhanced sensing of nucleic acids with silicon nanowire field effect transistor biosensors. *Nano Lett.* **2012**, *12*, 5262–5268. [[CrossRef](#)]
42. Bhattacharyya, I.M.; Ron, I.; Chauhan, A.; Pikhay, E.; Greental, D.; Mizrahi, N.; Roizin, Y.; Shalev, G. A new approach towards the Debye length challenge for specific and label-free biological sensing based on field-effect transistors. *Nanoscale* **2022**, *14*, 2837–2847. [[CrossRef](#)] [[PubMed](#)]
43. Palazzo, G.; De Tullio, D.; Magliulo, M.; Mallardi, A.; Intranuovo, F.; Mulla, M.Y.; Favia, P.; Vikholm-Lundin, I.; Torsi, L. Detection beyond Debye's length with an electrolyte-gated organic field-effect transistor. *Adv. Mater.* **2015**, *27*, 911–916. [[CrossRef](#)] [[PubMed](#)]
44. Garrote, B.L.; Fernandes, F.C.B.; Cilli, E.M.; Bueno, P.R. Field effect in molecule-gated switches and the role of target-to-receptor size ratio in biosensor sensitivity. *Biosens. Bioelectron.* **2019**, *127*, 215–220. [[CrossRef](#)]
45. Shao, W.; Shurin, M.R.; Wheeler, S.E.; He, X.; Star, A. Rapid Detection of SARS-CoV-2 Antigens Using High-Purity Semiconducting Single-Walled Carbon Nanotube-Based Field-Effect Transistors. *ACS Appl. Mater. Interfaces* **2021**, *13*, 10321–10327. [[CrossRef](#)] [[PubMed](#)]
46. Yakoh, A.; Pimpitak, U.; Rengpipat, S.; Hirankarn, N.; Chailapakul, O.; Chaiyo, S. Paper-based electrochemical biosensor for diagnosing COVID-19: Detection of SARS-CoV-2 antibodies and antigen. *Biosens. Bioelectron.* **2021**, *176*, 112912. [[CrossRef](#)]
47. Zamzami, M.A.; Rabbani, G.; Ahmad, A.; Basalah, A.A.; Al-Sabban, W.H.; Nate Ahn, S.; Choudhry, H. Carbon nanotube field-effect transistor (CNT-FET)-based biosensor for rapid detection of SARS-CoV-2 (COVID-19) surface spike protein S1. *Bioelectrochemistry* **2022**, *143*, 107982. [[CrossRef](#)] [[PubMed](#)]
48. Chen, P.H.; Huang, C.C.; Wu, C.C.; Chen, P.H.; Tripathi, A.; Wang, Y.L. Saliva-based COVID-19 detection: A rapid antigen test of SARS-CoV-2 nucleocapsid protein using an electrical-double-layer gated field-effect transistor-based biosensing system. *Sens. Actuators B Chem.* **2022**, *357*, 131415. [[CrossRef](#)]
49. Barra, M.; Tomaiuolo, G.; Vilella, V.R.; Esposito, S.; Liboa, A.; D'Angelo, P.; Marasso, S.L.; Cocuzza, M.; Bertana, V.; Camilli, E.; et al. Organic Electrochemical Transistor Immuno-Sensors for Spike Protein Early Detection. *Biosensors* **2023**, *13*, 739. [[CrossRef](#)]

**Disclaimer/Publisher's Note:** The statements, opinions and data contained in all publications are solely those of the individual author(s) and contributor(s) and not of MDPI and/or the editor(s). MDPI and/or the editor(s) disclaim responsibility for any injury to people or property resulting from any ideas, methods, instructions or products referred to in the content.